Insights into Cu(I) Exchange in HAH1 Using Quantum Mechanical and Molecular Simulations†

Bryan T. Op't Holt and Kenneth M. Merz, Jr.*

Department of Chemistry and Quantum Theory Project, 2328 New Physics Building, P.O. Box 118435, University of Florida, Gainesville, Florida 32611-8435

Received April 16, 2007; Revised Manuscript Received May 22, 2007

ABSTRACT: The human antioxidant protein, HAH1, is an important participant in a Cu(I) transport chain, delivering one Cu(I) ion to the Wilson's (WND) or Menkes disease protein (MNK). Full geometry optimizations and second-derivative calculations were performed on several binding site models using the B3LYP functional to derive parameters for the construction of a novel molecular mechanical (MM) force field for Cu(I) and its ligating residues in HAH1. MM minimization and molecular dynamics (MD) calculations were then performed using the AMBER suite to validate the newly generated force field. The X-ray crystal structure of the protein and the geometry of the Cu(I) binding site within the protein were reproduced by the MD simulations on the protein based on rmsd and visual inspection, validating the new force field parameters. The results from the quantum mechanical (QM) and MD simulations suggest that either a two- or three-coordinate exchange reaction is preferred and that it is unlikely that a four-coordinate Cu(I) species plays a role in copper exchange.

Because of its ability to readily cycle between oxidation states, Cu(I) is an important catalyst within the body. However, because of its high reactivity, Cu(I) is also prone to facilitating unhealthy side reactions in the body. One such reaction is the formation of toxic peroxide radicals. Hence, the concentration of Cu(I) is tightly regulated in biological systems. As a result, the $[Cu(I)]_{free}$ within the body has been estimated to be only 10^{-18} M, with $[Cu(I)]_{total}$ in the micromolar range (*1*, *2*), indicating that there are a significant number of high-affinity Cu(I) binding sites within a cell.

The Cu(I) transport pathway that involves the transmembrane multimetal transport protein hCtr1, the human antioxidant protein (HAH1 or Atox1), and the Wilson's (WND) or Menkes disease protein (MNK) is essential for the regulation of the availability of Cu ions within the body, in a process known as homeostasis (*2*−*11*). Problems within the copper transport structure of the cell result in Menkes syndrome, Wilson's disease, familial amyotrophic lateral sclerosis (fALS) disorders, and Alzheimer's disease (*3*). The proposed mechanism for the transfer of Cu(I) from HAH1 to its target protein suggests that the metal ion is passed from the donor to the target domain via a series of multicoordinate Cu(I) intermediates (*12*, *13*). Figure 1 illustrates the numerous possible copper coordination states, including a two-coordinate donor state, multiple three-coordinate states in which both the Cu donor and acceptor bind the ion, and the terminal product. Direct protein−protein contact between the donor and target is necessary for Cu(I) transfer to occur, and it has been suggested that the chaperone donates its metal ion in an enzymatic fashion, lowering the energy barrier for interprotein ion transport (*2*, *5*).

HAH1 is part of a family of copper-binding proteins that share a similar MT/CXXC Cu(I) binding motif. Cu(I) is bound to the metallochaperone via the S atoms of Cys residues in the binding loop. Wernimont et al. elucidated the structure of HAH1 using X-ray crystallography (PDB entry 1FEE) and determined the protein to be dimeric in the crystalline state, with one Cu(I) ion bound per dimer in a near-tetrahedral configuration (*13*). Although it was clear that Cu was bound by residues from each monomer, the data from the crystal structure supported either a four-coordinate or three-coordinate Cu(I) state with a loosely bound fourth residue (*12*). A four-coordinate Cu(I) site would also produce an electrostatic environment with a net charge of −3 in the active site, which is unfavorable (*13*). NMR studies performed by Anastassopoulou et al. concluded that Atx1, the yeast homologue of HAH1, exists as a monomer in solution, binding one Cu(I) ion per monomer in a nearly linear two-coordinate fashion (PDB entry 1TL4) (*14*). XAS data also suggested a two-coordinate Cu(I) site in the HAH1 monomer that would be amenable to further coordination to exogenous thiols and phosphines (*15*). It is believed that a monomer of HAH1 interacts favorably with the fourth domain of MNK during Cu(I) transfer due in part to the highly complementary structures of the donor and target along the protein−protein interface (*4*). The solution structure of the fourth domain of the Menkes ATPase, the target domain for transfer of Cu(I) from HAH1, was determined by Gitchier and co-workers in 1998 (*16*). A sequence analysis of numerous metal-transporting ATPases by Arnesano and co-workers revealed sequence homology between Atx1 and Ccc2, the yeast homologues of HAH1 and MNK, respectively. The primary structure similarity of the two proteins suggested that their comple-

† This work was supported by NIH Grant GM066859 to K.M.M.

* To whom correspondence should be addressed: Department of Chemistry and Quantum Theory Project, 2328 New Physics Building, P.O. Box 118435, University of Florida, Gainesville, FL 32611-8435. Telephone: (352) 392-6973. Fax: (352) 392-8722. E-mail: merz@qtp.ufl.edu.

10.1021/bi7007195 CCC: $37.00
Published on Web 07/06/2007

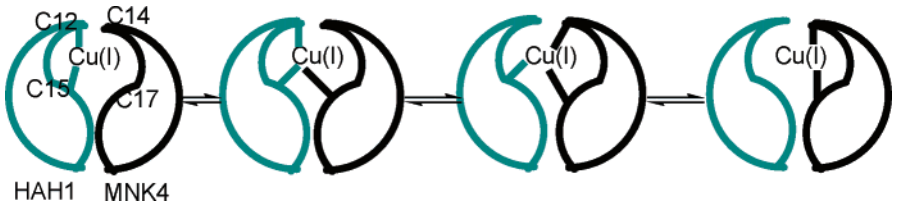

FIGURE 1: Proposed mechanism for transfer of Cu(I) between HAH1 and MNK4. A possible four-coordinate intermediate that would reside between the two three-coordinate states in the middle has been left out. In the HAH1 homodimer used as a mimic of the HAH1−MNK4 heterodimer in MD simulations, C14 and C17 of the target domain are replaced by Cys 12 B and Cys 15 B, respectively.

mentary tertiary structures could be important for inducing or facilitating Cu(I) transfer (*17*). Furthermore, since no crystal structure of the donor−target complex exists, Larin et al. used the solution structure of MNK4 and the crystal structure of HAH1 to artificially create a complex whose structure was compared to the X-ray structure of the HAH1 homodimer by rmsd that exhibited a high level of structural homology to the HAH1−MNK4 heterodimer (*18*). A similar docking study was undertaken by Arnesano in which the artificially docked Atx1−Ccc2 heterodimer was compared to available crystal structures of Atx1, Ccc2, and HAH1 (*19*). In this study, it was noted that the Atx1−Ccc2 complex, the yeast homologue of the human HAH1−MNK4 complex, is remarkably similar to the crystal structure of the HAH1 dimer as a whole and with respect to the geometry of the Cu(I) binding region of the heterodimer. In light of these studies, the use of the HAH1 homodimer structure as a model of the HAH1−MNK4 heterodimer is considered valid.

In 2006, Banci et al. released a collection of NMR structures of the Atx1−Ccc2 Cu(I) transfer complex (*20*). In light of this new structure, the solvent-exposed Cys residues of the metal binding site were identified as being more important than the Cys residues nearer the interface of the donor and target, and a "dominant" three-coordinate Cu(I) species was described in which Cu(I) is bound to the two solvent-exposed Cys residues and the buried Cys of the target domain (*21*). Furthermore, a nearby Lys residue was singled out as having a role in the accessibility of the binding site to the target domain and for forming important interactions with the metal-binding residues near the protein interface. The plausibility of a four-coordinate intermediate was further reduced due to the nature of the metal binding site in the NMR structures. While our work supports some of the conclusions drawn in these articles, the NMR structure of the Atx1−Ccc2 complex does not exclude other tricoordinate Cu(I) species in the Cu(I) transfer mechanism between HAH1 and MNK4.

The first goal of this work was to generate geometrically optimized structures of the models of the Cu(I) binding site of the HAH1 dimer in several Cu(I) coordination states and to calculate the bonding and charge parameters of the systems to create a molecular mechanics force field for the Cu(I) binding site in HAH1. The second phase of this work was to validate the new parameters by performing long time scale molecular dynamics simulations on the HAH1 homodimer as a model for the HAH1−MNK4 Cu(I) transfer heterodimer and to compare the results to the crystal structure of HAH1. MM calculations have been previously generated and reported for many transition metals, including Cu(II) (blue copper) (*22*), and there have been some reports of reliable MM Cu(I) force field parameters in the literature (*23*−*25*). Very recently, Dalosto published Cu(I) parameters for the

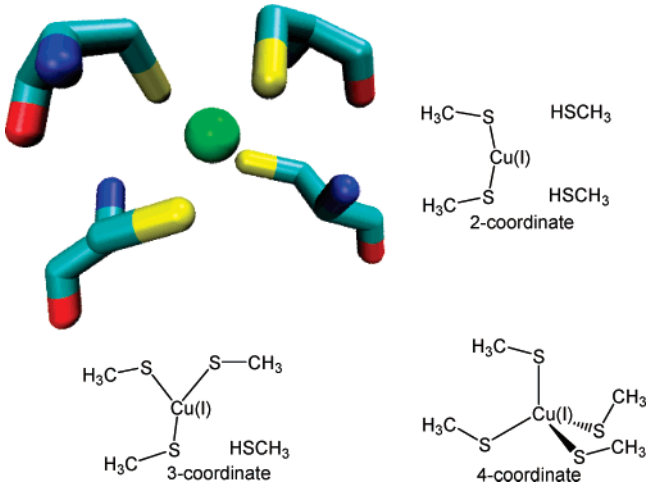

FIGURE 2: Cu(I) binding site from the HAH1 crystal structure, including Cys side chains, and the three QM models used to represent two-, three-, and four-coordinate Cu(I) environments.

Atx1 system based on quantum mechanical (QM)/molecular mechanical (MM) calculations (*23*). While the parameters published there are similar to those reported in this paper, our study incorporates dynamics, solvent interaction, and hydrogen bonding with the simulated protein, and energetics from QM calculations on model Cu(I) thiolate clusters to address the mechanism of Cu(I) transfer. The parameters presented here should be generally applicable to Cu(I) binding proteins that employ Cys residues to ligate the metal ion.

COMPUTATIONAL DETAILS

Ab initio calculations were performed on numerous multicoordinate models of the Cu(I) binding site from HAH1. Ligating Cys residues were contracted to methylthiolate (CH_3S^-) groups, and un-ionized Cys residues were reduced to methylthiols (CH_3SH). Three model clusters were generated on the basis of the X-ray crystal structure of the Cu(I) binding site from the HAH1 dimer. Those models include $Cu(I)(CH_3S^-)_4^{3-}$, $Cu(I)(CH_3S^-)_3[CH_3SH]^{2-}$, and $Cu(I)\text{-}(CH_3S^-)_2[CH_3SH]_2^-$. Gaussian 03, revision C.01 (*26*), was used to perform the calculations using the B3LYP (*27*−*30*) functional. Default grid spacing and convergence criteria were employed, and no symmetry constraints were applied. Cu(I) is a closed-shell system with electron configuration Ar[$3d^{10}$]. Therefore, singlet multiplicity was specified for each calculation. For C, H, and S atoms, the split-valence 6-311++G** basis set was employed (*31*−*33*), while the enhanced double-ζ basis set of Ryde (DZpdf) was used for Cu(I) (*34*). Figure 2 shows the X-ray crystal structure of the Cu(I) binding site of the HAH1 dimer, including Cys 12 and Cys 15 of both monomers. Also shown are the initial structures of the model

Table 1: Atom Type, Atomic Mass, van der Waals Radii, and van der Waals Well Depths for Cu(I) and Cu(I)-Bound S in HAH1

atom	atom type	mass (au)	van der Waals radius (Å)	well depth (ϵ) (kcal/mol)
two-coordinate structure				
Cu	PP	63.55	1.70	0.05
S (Cys 12 A)	SA	32.06	2.00	0.25
S (Cys 15 A)	SB	32.06	2.00	0.25
three-coordinate structure				
Cu	PP	63.55	1.70	0.05
S (Cys 12 A)	SA	32.06	2.00	0.25
S (Cys 15 A)	SB	32.06	2.00	0.25
S (Cys 12 B)	SC	32.06	2.00	0.25
four-coordinate structure				
Cu	PP	63.55	1.70	0.05
S (Cys 12 A)	SA	32.06	2.00	0.25
S (Cys 15 A)	SB	32.06	2.00	0.25
S (Cys 12 B)	SC	32.06	2.00	0.25
S (Cys 15 B)	SD	32.06	2.00	0.25

Table 2: Bond Lengths, Bond Angles, and Associated Force Constants for the HAH1 Cu(I) Binding Site

bond	k_{bond} (kcal mol^{-1} Å^{-2})	r_0 (Å)
Cu−S	60.00	2.19
CT−S	219.3	1.84
angle	k_t (kcal mol^{-1} rad^{-2})	θ_0 (deg)
S−Cu−S	50.00	109.5
C−S−Cu	93.98	95.91

clusters that were used. The models were created using WebLab ViewerPro, version 3.7 (*35*). Force constant calculations were performed on the geometry-optimized models using internal coordinates and the IOp(7/33=1) keyword. Charge populations were also determined from the optimized structures using the Merz−Kollman−Singh method (*36*, *37*), and the IOp(6/32=2) keyword. Default van der Waals radii were used for all atoms except Cu(I), for which a radius of 0.91 Å was specified on the basis of the crystal radius of an O_h Cu(I) ion (*38*).

Simulations were performed in AMBER (*39*) using the 1994 parameter set of Cornell et al. for the protein atoms (*40*). The X-ray crystal structure of the HAH1 dimer was used as the starting structure for the force field-based simulations. New atom types were specified for the Cu(I) ion and any Cu-binding S atoms. Force field parameter files were created for each of the new atom types. Mass, bonding, angular, torsion, and nonbonding parameters for Cu(I) and for Cu-bound S are listed in Tables 1 and 2. Default charges were used for all atoms except Cu(I) and for atoms within the Cu-binding residues. Charges for those atoms were adapted from the MKS potentials generated in Gaussian 03. The *espgen* and *respgen* programs in the *antechamber* package within AMBER were used to convert the charges into AMBER format. These charges were modified to ensure integer charges on the systems, and the same charges for Cu(I) and Cu(I)-bound Cys residues were imposed in the MD simulations regardless of the coordination state of the metal ion. The total electrostatic potential-derived charge of a Cu-bound Cys residue was approximately −1.1, and the charge imposed on Cu(I) was +1.36. AMBER ESP charge values are listed in Table 3. The apo-HAH1 dimer is neutral, so the total charges of the Cu(I)-bound protein systems are equal to that of the Cu(I) binding site alone.

Table 3: Cys and Cu(I) RESP Charges Used for the HAH1 Cu(I) Binding Site

atom	Cys charge	atom type	RESP charge in AMBER
N	−0.4157	N	−0.3630
H	0.2719	H	0.2520
C_α	0.0213	CT	0.0350
H_α	0.1124	H1	0.0480
C_β	−0.1231	CT	−0.5720
H_β	0.1112	H1	0.2440
S_γ	−0.3119	SA, SB, SC, or SD	−1.0918
C	0.5973	C	0.6160
O	−0.5679	O	−0.5040
H_γ	0.1933	HS	not applicable
Cu	not applicable	PP	1.3673

Although the Cu−S bond lengths were shorter in the gas-phase QM models than in the crystal structure, the force constants calculated in Gaussian 03 were found to be too weak to reproduce the binding site geometry of the HAH1 crystal structure during MD simulations. Therefore, the initial QM force constants were increased to the values shown in Table 3 to ensure that the Cu(I)−S distances closely reproduced those seen in the HAH1 homodimer. C_β−S bond lengths were taken from the QM models, and bond force constants were based on CT−SH values in the 1994 force field (219.3 and 237 kcal/mol). H_β−C_β−S and C_β−S−Cu angles and bending force constants were taken from the QM model data. S−Cu−S angle values were also taken from the QM model data, with the angle force constants resembling those of the H_β−C_β−S angle in the 1994 force field (50.0 and 43.0 kcal mol^{-1} rad^{-2}, respectively). Torsion values were modified slightly from the 1994 parameter library for Cys. S was given a nonbonding radius of 2.00 Å and a well depth of 0.25 kcal/mol. The copper(I) ion was given a nonbonding radius of 1.70 Å and a well depth of 0.05 kcal/mol. The van der Waals parameters for S are the same as those in the parm94 library, and the well depth values for Cu(I) are comparable to those in the parm91 library. The hard sphere radii in the Cu(I) nonbonding parameters are larger in comparison to both the AMBER parm91 value of 1.2 Å and that of 1.09 Å used by Dalosto (*23*). The larger radius used in these simulations was used to ensure that any S or H atoms from nearby unbound Cys residues did not interfere with the metal center.

Initial gas-phase MM minimizations were performed on the Cu(I)-bound dimer with *sander* using the default minimization algorithm for 2000 steps. The nonbonded cutoff was set to 20.0 Å. Minimization was followed by a series of temperature equilibration MD simulations during which the temperature of the system was increased from 100 to 300 K. Upon temperature equilibration, long time scale MD simulations were performed at a constant temperature of 300 K using the Berendsen algorithm (*41*). The gas-phase temperature-equilibrated structures were then surrounded by an 8.0 Å TIP3P water box for solvent-phase MD simulations. The solvated system was minimized with a nonbonded cutoff of 8.0 Å using the default minimization method for 8000 steps. Again, the temperature of the system was brought to 300 K over a series of MD simulations. SHAKE was implemented for bonds involving hydrogen. Long time scale constant-pressure MD simulations were performed on the equilibrated systems at 300 K with periodic boundary

conditions in place. The reported MD runs were at least 3600 ps in length, using a time step of 2.0 fs.

Five different Cu(I)-bound HAH1 dimers were simulated in this study, with each system mimicking a potential intermediate in the Cu(I) transport mechanism from the HAH1 monomer to MNK4. The five systems differed in the Cu(I) coordination state and the identity of the Cu(I)-binding residues. The four-coordinate system is nearly identical to the crystal structure of Cu(I)-bound HAH1, with Cu(I) being bound by Cys 12 and Cys 15 from monomer A and by Cys 12 and Cys 15 from monomer B. Two three-coordinate systems included Cu(I) bound to Cys 12 A, Cys 15 A, and Cys 12 B (termed 3-coord A) and Cu(I) bound to Cys 12 A, Cys 15 A, and Cys 15 B (termed 3-coord B). Two two-coordinate systems were as follows: Cu(I) bound to Cys 12 A and Cys 15 A (termed 2-coord) and Cu(I) bound to Cys 15 A and Cys 15 B (termed 2-coord-bridged). The *ptraj* program in AMBER was used to evaluate the validity of the new Cu(I) and S force field parameters on the basis of the geometries of the five HAH1 dimer systems compared to the crystal structure of the dimer. Root-mean-square deviation (rmsd), rms fluctuation (rmsf), protein/solvent radial distribution functions, and radii of gyration were calculated for each of the five HAH1 systems.

RESULTS AND DISCUSSION

Potential intermediates in the multicoordinate transport mechanism for Cu(I) include some two- and three-coordinate metal sites, with the possibility of a four-coordinate Cu site. To assess the relative energies of these three different coordination states, single-point energy calculations were performed on the gas-phase optimized model clusters both in the gas phase and with implicit aqueous solvent. The energies of two model clusters cannot be directly compared since the number of atoms of each model decreases as the coordination number of Cu increases. Therefore, the energies of two isodesmic reactions were calculated to gauge the energy difference between different coordination states.

3-coordinate to 4-coordinate

$$Cu(I)[(SCH_3)^-]_3[HSCH_3]^{2-} + H_2O \rightarrow Cu(I)[(SCH_3)^-]_4^{3-} + H_3O^+$$

2-coordinate to 3-coordinate

$$Cu(I)[(SCH_3)^-]_2[HSCH_3]_2^- + H_2O \rightarrow Cu(I)[(SCH_3)^-]_3[HSCH_3]^{2-} + H_3O^+$$

The single-point energy of each molecule or ion in the isodesmic reactions was calculated separately before the ΔE_{rxn} was determined. The relative energies for the reactions above are listed in Table 4 and plotted in Figure 3. On the basis of the relative QM energies of the different model clusters, the four-coordinate state is shown to be energetically unfavorable. Table 4 gives the electronic energies of the products and reactants in Hartrees and the ΔE_{rxn} values for both gas- and solvent-phase reactions in Hartrees and kilocalories per mole. As expected, $\Delta E_{rxn}^{solvent}$ is stabilized relative to the gas-phase value for both reactions. For the two-coordinate to three-coordinate reaction and the three-coordinate to four-coordinate reaction, ΔE_{rxn}^{gas} is 244 and 330 kcal/mol, respectively. For the solvent-stabilized reactions, $\Delta E_{rxn}^{solvent}$ is 47.7 kcal/mol for the two- to three-coordinate reaction and 63.8 kcal/mol when creating the four-coordinate state from the three-coordinate state. Overall, the four-coordinate state is 111 kcal/mol higher in energy than the two-coordinate state in implicit aqueous solvent. Higher-energy transition states, not shown here, may exist between the different cluster models. These ΔE_{rxn} calculations support the hypothesis that a potential four-coordinate intermediate in the Cu(I) transport mechanism between HAH1 and MNK4 is not likely to exist due to the comparatively larger energy difference between the three-coordinate and four-coordinate states over the two-coordinate to three-coordinate states.

Table 4: E and ΔE Values for Gas-Phase and Solvated Model Clusters[a]

	2-coord	H_2O	3-coord	H_3O^+
E^{gas}	−3394.453	−76.444	−3393.791	−76.718
$E^{solvent}(\epsilon=80)$	−3394.524	−76.460	−3394.050	−76.858
$\Delta E_{rxn}^{solvent}$	0.0759	47.7 kcal/mol		
ΔE_{rxn}^{gas}	0.389	244 kcal/mol		

	3-coord	H_2O	4-coord	H_3O^+
E^{gas}	−3393.791	−76.444	−3392.992	−76.718
$E^{solvent}(\epsilon=80)$	−3394.050	−76.460	−3393.551	−76.858
$\Delta E_{rxn}^{solvent}$	0.102	63.8 kcal/mol		
ΔE_{rxn}^{gas}	0.525	330 kcal/mol		

[a] Energies given in hartrees except where indicated.

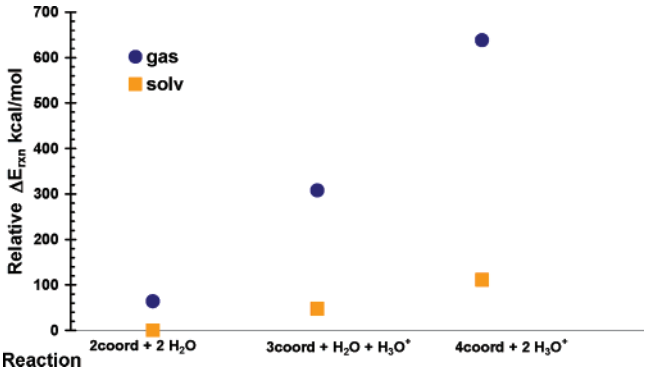

FIGURE 3: Relative energies for the species involved in the isodesmic reactions of an increasing level of Cu(I) coordination by addition of methylthiolate residues. Protons donated by methylthiols are released to solvent at an infinite distance as they are bound by the metal ion.

The QM calculations do not take into account the effect of the protein environment on Cu(I) transport. Moreover, the symmetrical nature of the QM clusters excludes the possibility of creating different two-coordinate or three-coordinate states. In the protein, there are many different possible two-coordinate and three-coordinate states that can be investigated with molecular mechanics methods. Performing such calculations required the creation of parameters for the Cu(I) ion and its ligating residues.

Table 5 lists the geometrical parameters about the Cu center for the three QM model clusters. Bond lengths and bond angles generated by geometry optimization of each cluster were collected for inclusion in the MM force field. Force constants for Cu−S bonds and the electrostatic potentials, based on the optimized geometries of the clusters, were also collected for inclusion in the new set of Cu(I) MM

Table 5: Geometry Parameters of the DFT-Optimized Multicoordinate Models

model	Cu−S (Å)	Cu−S (Å)	Cu−S (Å)	Cu−S (Å)	S−Cu−S (deg)	C−S−Cu (deg)
2-coord	2.23	2.23	5.25	6.00	180.0	101.8
3-coord	2.31	2.35	2.41	4.98	114.6	105.2
4-coord	2.19	2.19	2.19	2.24	109.5	108.9

Table 6: Comparison of the HAH1 Active Site between the Four-Coordinate Model, the Solvated, Equilibrated Protein, and the X-ray Crystal Structure of the Cu(I)-Bound Protein

parameter	QM model	protein	X-ray
Cu−S (Cys 12 A)	2.19 Å	2.29 Å	2.30 Å
Cu−S (Cys 15 A)	2.19 Å	2.14 Å	2.39 Å
Cu−S (Cys 12 B)	2.19 Å	2.33 Å	2.30 Å
Cu−S (Cys 15 B)	2.24 Å	2.39 Å	2.32 Å
Cys 12 A−Cu−Cys 15 A	109.0°	117.5°	115.7°
Cys 12 A−Cu−Cys 12 B	109.5°	112.5°	109.4°

parameters. It can be seen that Cu−S distances for unbound methylthiols are more than 4.98 Å from the metal ion, and that Cu−S bond lengths are on the order of 2.2−2.3 Å. The bond angles also conform to experimental results. The 180° S−Cu−S bond angle in the two-coordinate model agrees with the NMR structure of Atx1, and bond angles in the four-coordinate model reveal near-tetrahedral geometry, which agrees with the X-ray structure of HAH1. There is no NMR or X-ray evidence of a three-coordinate state, although such a state has been suggested by EXAFS data of Atx1 (*42*), or that the Cu environment would be nearly trigonal planar, which the QM model supports as well.

The four-coordinate HAH1 system was the first to be simulated using the newly created parameters listed in Tables 1−3. Table 6 compares Cu−S bond lengths and S−Cu−S bond angles for the four-coordinate QM model cluster, the four-coordinate simulated system, and the active site geometry from the HAH1 crystal structure. It shows that the Cu−S bond lengths are shorter in the gas-phase QM model than in either the crystal structure or the solvent-phase MD-simulated system, and that the geometrical parameters for the simulated protein adequately match those of the crystal structure. Results from the analyses of the trajectories of all five MD-simulated structures are listed in Table 7.

Four rmsd values are listed in Table 7. There are two values that encompass the entire protein and two values that focus only on the Cu-binding loop of HAH1. It can be seen that all-atom rmsd values are below 2.70 Å for all five systems and that the geometries of the binding loops of each system are indistinguishable from that of the crystal structure as binding loop rmsd values are all close to 1.00 Å. These rmsd values showcase the ability of the new parameters to replicate the geometry of the crystal structure of the whole protein and, more importantly, that of the metal binding site.

The rmsf values listed in Table 7 reveal details about the flexibility of certain residues as well as the complete protein and the protein backbone for the three models. The small difference between rmsf values for the complete protein compared to the backbone suggests that the flexibility of the protein is not limited to the side chains and that the backbone also moves freely. From the rmsf data for Cu(I)-binding residues Cys 12 A, Cys 15 A, Cys 12 B, and Cys 15 B, it appears that Cys 12 A and Cys 12 B have comparable magnitudes in each model. The values for Cys 15 A and Cys 15 B are also similar for each model. The similarity is derived from the location of these residues on the binding loop. Cys 12 A and Cys 12 B are more solvent-exposed and move more freely due to solvent interactions and being farther from the monomer interface. On the other hand, Cys 15 A and Cys 15 B show less flexibility as they are close to the interface region and not generally solvent-exposed. The flexibility of the Cys 12 residues may play a role in the transfer of Cu(I) between binding domains. The rmsf data for Cu(I) show that Cu(I) is least mobile when bound by only three residues. In the four-coordinate model, Cu(I) and its ligands are more flexible. We hypothesize that this is observed because the four-coordinate Cu(I) complex is more strained than the three-coordinate system. In other words, the structure is preorganized to bind, or is designed to stabilize, the three-coordinate state over the four-coordinate one. Evidence of this is seen in the rmsf data for each of the four Cu-binding residues in the four-coordinate model. Cys 12 A and Cys 12 B, which are close to the protein surface, are seen to be more flexible than Cys 15 A and B which are farther from solvent in the monomer−monomer interface. Moreover, the overall protein rmsf is greatest for the four-coordinate state.

Table 7: Summary of rms Deviations, rms Flexibilities, and Radii of Gyration for the Five Solvated HAH1 Protein Models and Key Active Site Residues

	2-coord	2-coord-bridge	C12 B bound 3-coord B	C15 B bound 3-coord A	4-coord
		rmsd (Å)			
total	2.69	2.67	2.27	2.10	2.04
backbone	1.89	1.88	1.30	1.34	1.17
binding loop	0.89	1.29	0.87	0.94	1.31
binding loop backbone	0.34	0.71	0.37	0.38	0.54
		R_g (Å)			
protein average	29.38	27.26	29.35	29.30	29.43
		rmsf (Å)			
total	4.98	4.85	3.60	4.54	5.46
backbone	4.80	4.70	3.46	4.37	5.23
Cu	5.11	2.66	2.19	4.19	3.94
Cys 12 A	5.28	3.83	2.40	4.95	5.08
Cys 15 A	4.10	2.66	1.78	4.38	3.45
Cys 12 B	6.14	3.62	3.44	3.64	4.68
Cys 15 B	4.32	2.15	1.88	2.60	3.21

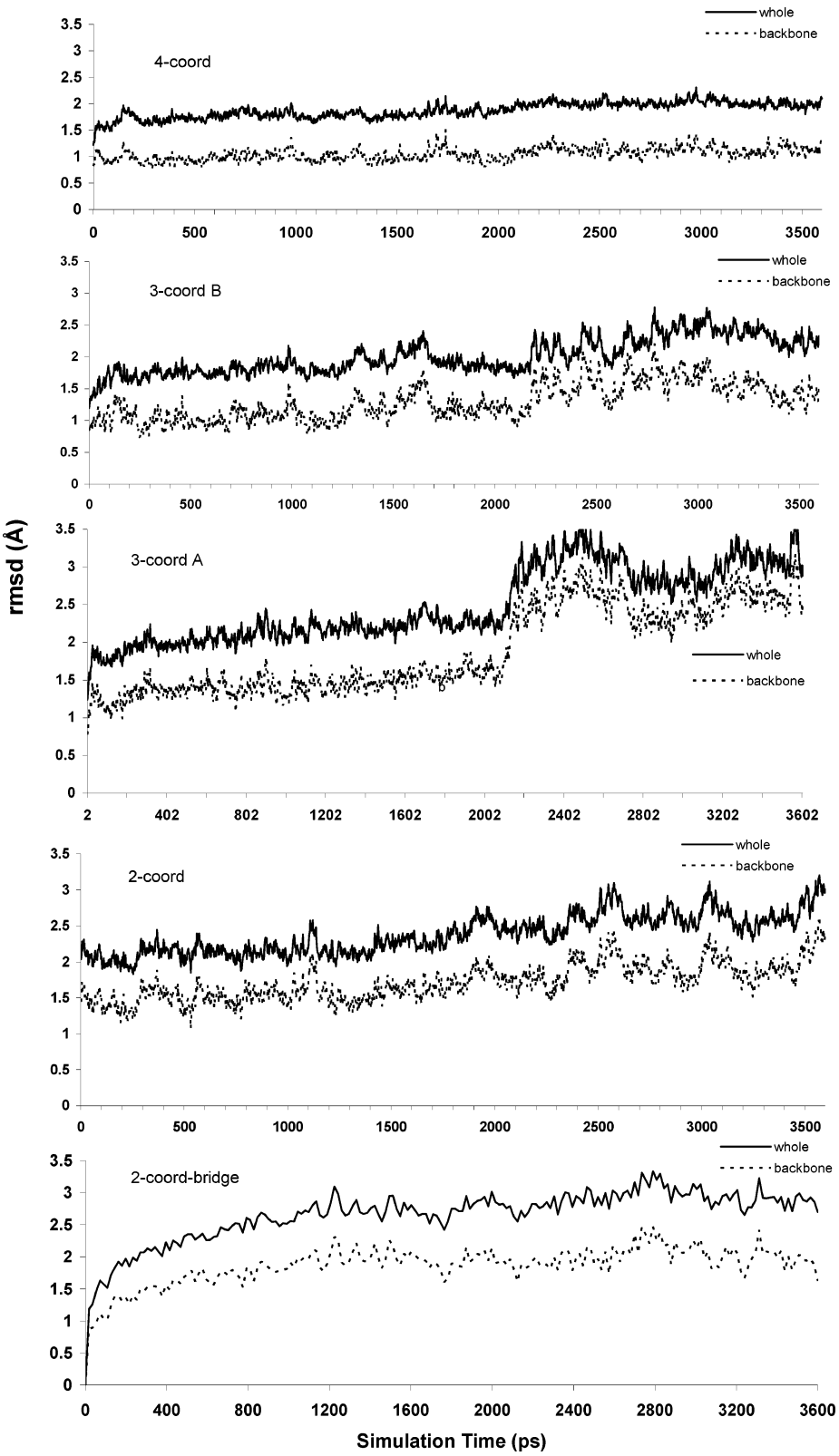

FIGURE 4: Whole-protein rmsd plots for the five solvated protein systems. Plots include all-atom rmsd values and backbone atom-only values.

Figures 3 and 4 display the rmsd plots of the five simulated systems. The figures show that the active site regions of all five models apparently reached an equilibrium state after ~400 ps, and while the entire protein is generally in good agreement with the crystal structure throughout, the complete protein structure did take longer to reach an equilibrium state. For the whole-protein models, rmsd values between 2.0 and 2.5 Å were achieved by 2500 ps and were maintained beyond that point in the simulations.

One interesting observation from the simulations of the solvated protein systems was the behavior of the Cu-binding residues in the 2-coord-bridged, 3-coord A, and 3-coord B systems. Cys side chains have the ability to form hydrogen bonding interactions with the solvent around the protein. The

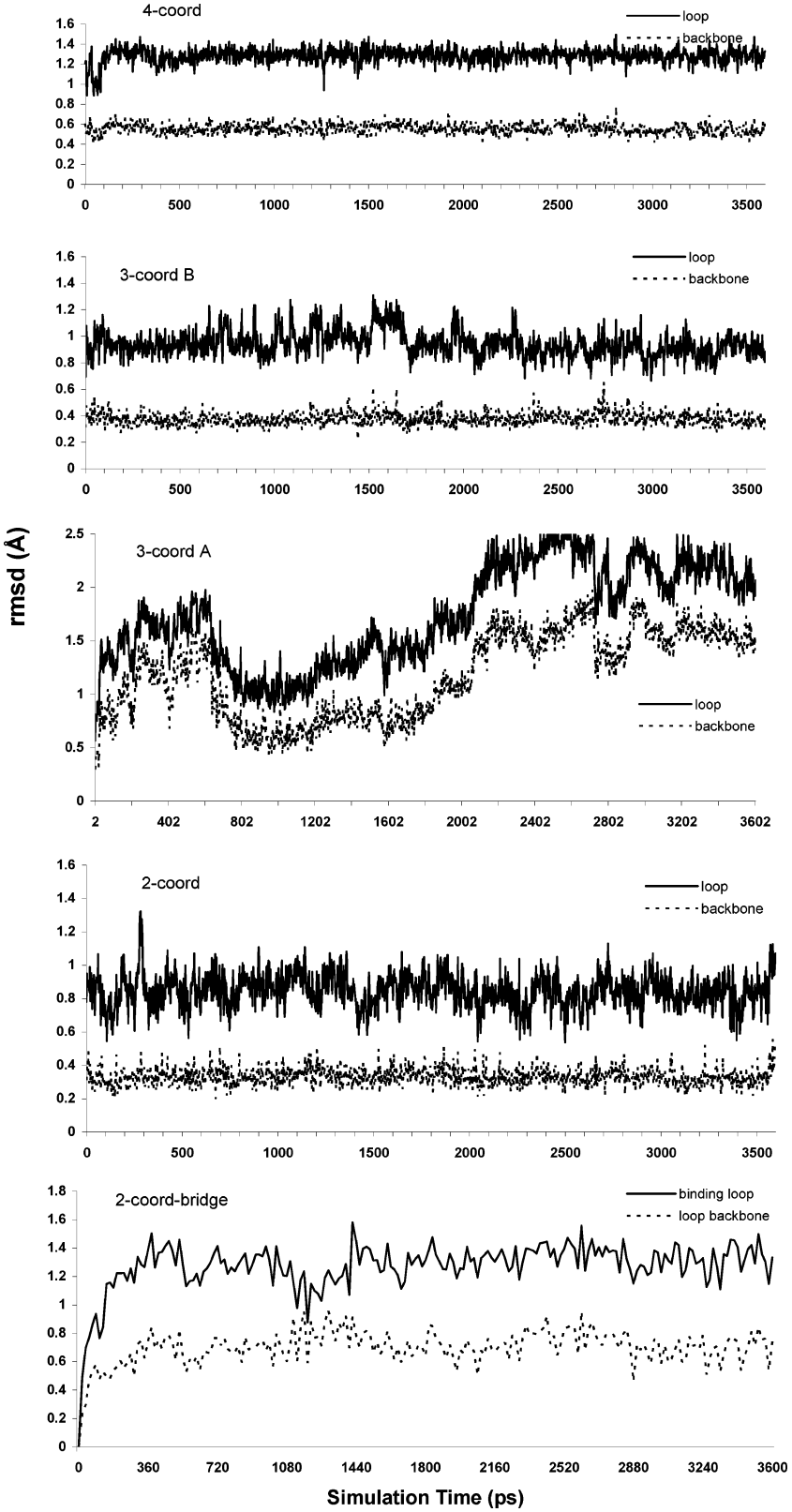

FIGURE 5: Considering only the binding motifs of the two monomers (Met10−Cys15), all-atom and backbone-only rmsd plots are shown for the five solvated protein systems.

Cu binding site of the HAH1 monomer exists on a solvent-exposed loop. In the HAH1 dimer, the protein−protein interface prohibits Cys 15 A and Cys 15 B from interacting with the solvent. However, Cys 12 A and Cys 12 B are still able to contact the solvent. Figure 5 shows the orientation of the Cys residues in 3-coord A and 3-coord B after MD simulation for 3600 ps. It can be seen that when Cys 15 B is bound to Cu along with the two Cys residues from monomer A, then Cys 12 B is left to interact with the solvent. However, when Cys 12 B is bound to Cu along with the two Cys residues from the monomer, then Cys 15 B is not able to form any favorable solvent contacts. Rather, the unbound Cys 15 B is buried deeper in the monomer−monomer interface. Similarly, in the 2-coord-bridged system,

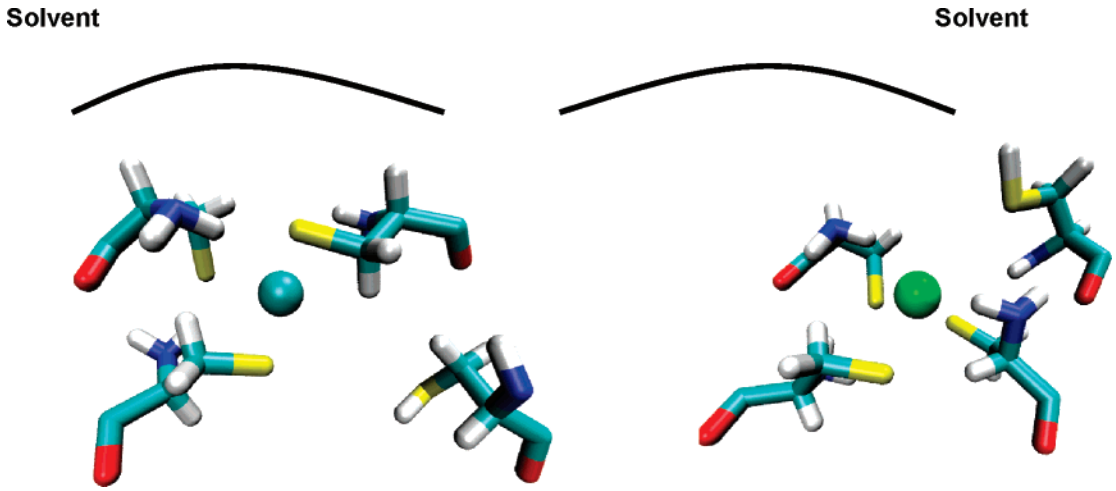

FIGURE 6: Snapshots of the 3-coord A (left) and 3-coord B (right) solvated protein Cu(I) binding sites after simulation for 3600 ps at 300 K. The unbound Cys residue in the 3-coord A system (Cys 15 B) moves away from the metal ion and away from solvent, while the unbound residue in the 3-coord B system (Cys 12 B) also moves away from the metal ion, but toward solvent.

where both Cys 15 A and Cys 15 B are Cu-bound, Cys 12 A and Cys 12 B freely interact with the solvent. We believe that favorable Cys−solvent interactions may play a role in determining the manner in which the target domain binds to the incident Cu ion during transfer.

To determine the average proximity to solvent of the Cys side chains in the Cu(I) binding site, protein−solvent radial distribution functions were calculated. Figure 7 shows $g(r)$ plots for the five multicoordinate HAH1 MD simulations. Each plot represents a series of snapshots between 1500 and 3000 ps during the MD simulation. The plot for the four-coordinate structure shows that the Cys 15 B side chain is farther from the solvent than any of the other three Cu-bound residues, with Cys 12 B maintaining the highest population of solvent molecules within 4 Å of the terminal S atom. The plots for the 3-coord A and 3-coord B models are much different in the region from 0 to 10 Å. In the 3-coord A structure, Cys 15 B is unbound from Cu, yet as the $g(r)$ plot shows, water is unable to penetrate into the protein to hydrogen bond with Cys 15 B even when compared to the three Cu-ligating residues, including buried residue 15 A. Conversely, the plot for the 3-coord B protein reveals that when the surface-exposed Cys 12 B is unbound from Cu, its side chain comes in (not unexpectedly) close contact with solvent. This is represented by a broad peak in the $g(r)$ plot from 3 to 6 Å from the S atom on Cys 12 B and a peak between 1.5 and 3 Å for the terminal H of that residue. The location and magnitude of the S and H peaks on 3-coord B relative to those on 3-coord A suggest that Cys 12 B readily forms favorable solvent contacts when it is not bound to the metal ion and that the Cys 15 B side chain is not capable of such interactions and might be less likely to become unligated with Cu(I). A similar comparison can be made in the two-coordinate radial distribution plot. It can be seen that the magnitude of the Cys 15 A S peak is much larger than that of the Cys 15 B S peak. This suggests that even when Cys 15 B is not bound to Cu, it is still less accessible to solvent than Cys 15 A which is complexed to copper. Another feature of the two-coordinate plot is that unbound S atoms produce curves different from those of the bound S atoms. In the two-coordinate model, only residues from monomer A are bound to Cu. It can be seen that the $g(r)$ plots from the two S atoms on monomer A resemble each other. S atoms from monomer B produce a different set of similar peaks. The curves for the S atoms in the Cu-bound residues (Cys 15 A and 15 B) in the two-coord-bridged $g(r)$ plot closely resemble each other. However, some unexpected dissimilarities exist when the peaks from Cys 12 A and Cys 12 B are compared. While the peaks from the Cu-bound S atoms maintain their similarity throughout the range of 0−15 Å, the peaks for unbound S atoms and their accompanying H atoms are similar in shape, but not in magnitude for distances of <6 Å. S and H from Cys 12 B have much higher solvent populations with 5 Å than the same atoms from Cys 12 A. In fact, H atoms from Cys 12 A show no solvent population with 4 Å. The lower peaks for the H atoms in the two-coord-bridged structure could reflect interactions between the hydrogens and the Cu-binding S atoms on the spatially adjacent Cys 15 residues on each monomer, or it could suggest that when the two HAH1 monomers share a Cu bridge in the two-coordinate state, the coordination unsaturated metal ion attempts to form bonds with the unbound Cys residues nearby.

Hydrogen bonding networks for Cys 15 A and Cys 15 B were studied from protein structures at the end of the MD simulations. The Lys 60 side chains of both monomers are arranged such that they interact closely with Cys 15 A and Cys 15 B at the bottom of the binding site. In the two-coordinate system, the distances between the S atom of Cys 15 A and the H atom from the end of Lys 60 A and Lys 60 B are 2.03 and 2.17 Å, respectively, suggesting strong H-bonding interactions between the two atoms. Likewise, the two-coord-bridged structure reveals that S atoms from both Cys 15 A and Cys 15 B are H-bonded to Lys 60 A and Lys 60 B. In this case, Lys 60 A interacts with both Cys 15 A and Cys 15 B, with S−H distances of less than 1.9 Å. Lys 60 B interacts with Cys 15 B at a distance of 1.95 Å. The three-coordinate systems also exhibit H-bonding between these lysines and the cysteines in the binding site. In the 3-coord A system, while Cys 12 B is interacting with solvent at the protein surface, Cys 15 B is bound to Cu and shares a H-bonding interaction with Lys 60 B some 1.92 Å away. Cys 15 A is also 1.92 Å from Lys 60 B but is also only 2.06 Å from Lys 60 A. Both the hydrogen bonding network of Cys 15 B to lysine and that of Cys 12 B to solvent in the 3-coord A model are favorable when compared to the

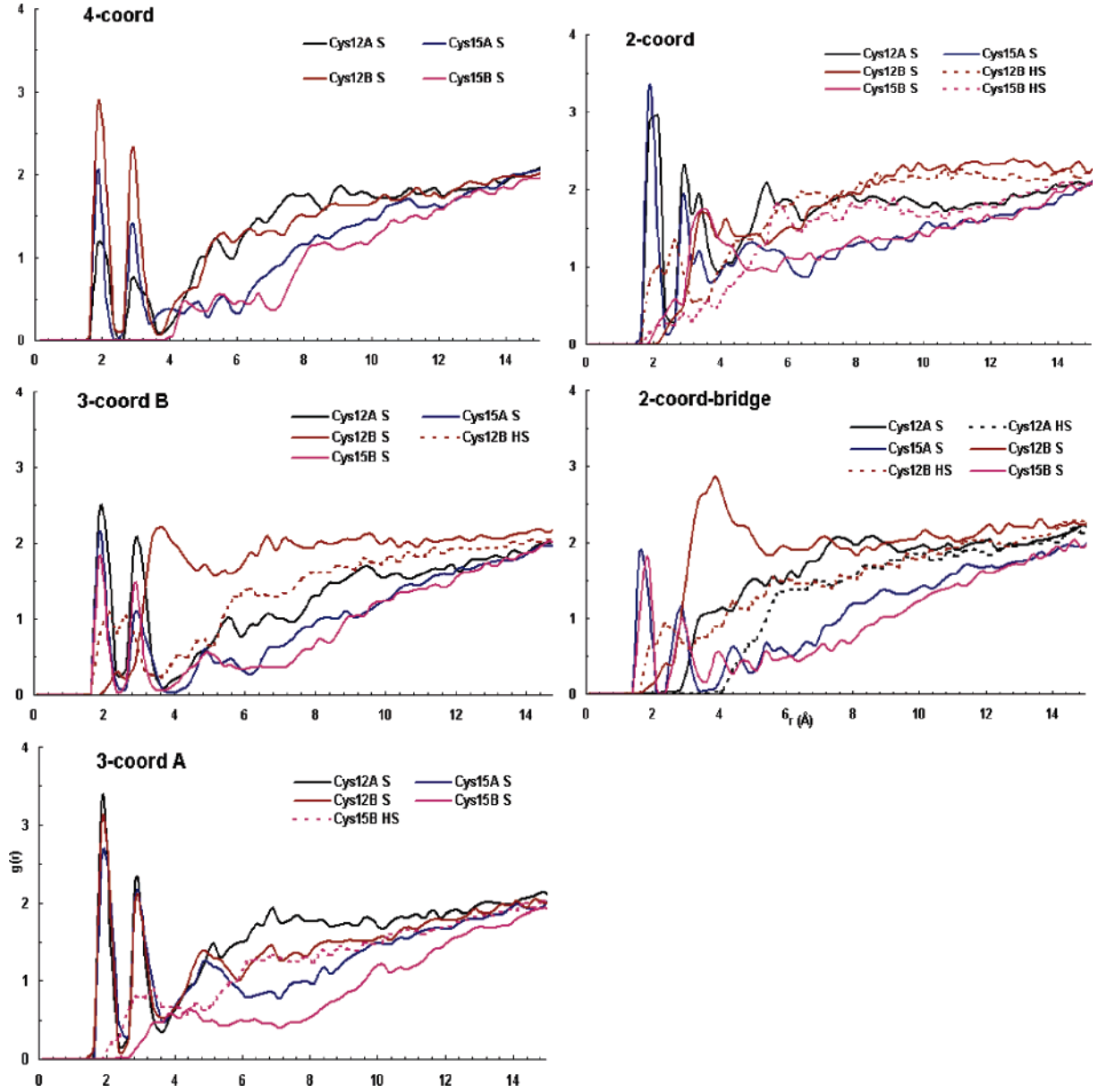

FIGURE 7: Radial distribution plots for protein−solvent interactions for the five different Cu(I) coordinations of the simulated HAH1 dimer active site. $g(r)$ is plotted from 1500 to 3000 ps for each of the simulation windows described above, representing protein−solvent interactions in the equilibrated systems.

arrangements observed in the 3-coord B model. The 3-coord B model, with Cys 12 B bound to Cu and Cys 15 B unbound, shows no H-bonding between Cys 15 B and any lysine. Furthermore, Cys 12 B has no contact with either the solvent or a lysine residue. Cys 15 A experiences H-bonding to both Lys 60 A and Lys 60 B. Hydrogen bonding in the 4-coord structure is most similar to that of the 3-coord A system, with Cys 15 A and Cys 15 B interacting with Lys 60 A and Lys 60 B. However, in this case, Cys 12 B has no solvent interactions as in 3-coord A.

The combination of the solvent interactions shown by Cys 12 B with the H-bonding interactions observed with Cys 15 A and Cys 15 B in the HAH1 dimer model strengthens the suggestion that Cys 17 of the target MNK4 domain will bind Cu first in the transfer mechanism between HAH1 and MNK4.

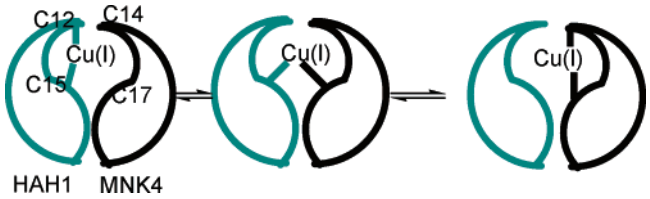

FIGURE 8: Proposed mechanism for transfer of Cu(I) between HAH1 and MNK4 involving only two-coordinate thiolate−Cu(I) species.

CONCLUSION

The QM calculations conducted in the first part of this work created a foundation for the description of the Cu(I) binding site in HAH1. The main conclusion is the four-coordinate state is very energetically unfavorable and is probably an unlikely candidate for an intermediate along the reaction profile that involves exchanging ligating Cys residues around Cu(I). Moreover, the two- to three-coordinate

transfer involves a large energetic penalty, but we suspect that the protein environment can play a role in decreasing this energy difference quite significantly. Future QM/MM studies can better address this observation. The results from the MD simulations of the three Cu(I)-bound HAH1 dimer models show that the QM-derived parameters used to construct the MM force field adequately described the system on the basis of comparisons to the HAH1 crystal structure. The rmsd data show that the computationally generated structures maintain the same fold and Cu(I) structure as the X-ray-derived protein structure. After the MD simulations were completed, the question of deciphering the order of Cu(I) binding and release during Cu(I) transfer remains to be answered, but several hypotheses can be derived.

If one assumes that the protein environment cannot stabilize the exchange reaction sufficiently, then one can propose a two-coordinate-only ligand exchange process. This proposal is given in Figure 8. Otherwise, the proposal in Figure 1 appears to be the best hypothesis based on the MD simulations in that the surface-exposed Cys residues (12 A and 12 B) can be best stabilized by solvation effects while they interchange from the thiolate ↔ thiol forms along the reaction pathway and Cys residues (15 A and 15 B) maintain a stabilizing hydrogen bonding network with nearby Lys residues (60 A and 60 B). QM/MM studies aimed at refining the overall reaction profile in terms of the stability of two- and three-coordinate intermediates would aid in discriminating between these two pathways.

ACKNOWLEDGMENT

We thank Amy Rosenzweig and Mike Weaver for helpful comments and suggestions.

REFERENCES

1. Rae, T. D., Schmidt, P. J., Pufahl, R. A., Culotta, V. C., and O'Halloran, T. V. (1999) Undectectable Free Copper: The Requirement of a Copper Chaperone of Superoxide Dismutase, *Science 284*, 805−808.
2. O'Halloran, T. V., and Culotta, V. C. (2000) Metallochaperones, an Intracellular Shuttle Service for Metal Ions, *J. Biol. Chem. 275*, 25057−25060.
3. Gaggelli, E., Kozlowski, H., Valensin, D., and Valensin, G. (2006) Copper Homeostasis and Neurogenerative Disorders (Alzheimer's, Prion, and Parkinson's Diseases and Amyotrophic Lateral Sclerosis), *Chem. Rev. 106*, 1995−2044.
4. Harrison, M. D., Jones, C. E., Solioz, M., and Dameron, C. T. (2000) Intracellular Copper Routing: The Role of Copper Chaperones, *Trends Biochem. Sci. 25*, 29−32.
5. Huffman, D. L., and O'Halloran, T. V. (2001) Function, Structure, and Mechanism of Intracellular Copper Trafficking Proteins, *Annu. Rev. Biochem. 70*, 677−701.
6. Lieberman, R. L., and Rosenzweig, A. C. (2004) Metal Ion Homeostasis, in *Comprehensive Coordination Chemistry II: From Biology to Nanotechnology*, 1st ed., Elsevier Pergamon: Amsterdam and Boston, pp 195−211.
7. Puig, S., and Thiele, D. J. (2002) Molecular Mechanisms of Copper Uptake and Distribution, *Curr. Opin. Chem. Biol. 6*, 171−180.
8. Hamza, I., Schaefer, M., Klomp, L. W. J., and Gitlin, J. D. (1999) Interaction of the copper chaperone HAH1 with the Wilson disease protein is essential for copper homeostasis, *Proc. Natl. Acad. Sci. U.S.A. 96*, 13363−13368.
9. Mercer, J. F. B., Barnes, N., Stevenson, J., Strausak, D., and Llanos, R. M. (2003) Copper-induced trafficking of the Cu-ATPases: A key mechanism for copper homeostasis, *BioMetals 16*, 175−184.
10. Valentine, J. S., and Gralla, E. B. (1997) Delivering Copper Inside Yeast and Human Cells, *Science 278*, 817−818.
11. Tanchou, V., Gas, F., Urvoas, A., Cougouluègne, F., Ruat, S., Averseng, O., and Quéméneur, E. (2004) Copper-mediated homodimerisation for the HAH1 metallochaperone, *Biochem. Biophys. Res. Commun. 325*, 388−394.
12. Rosenzweig, A. C. (2001) Copper Delivery by Metallochaperone Proteins, *Acc. Chem. Res. 34*, 119−128.
13. Wernimont, A. K., Huffman, D. L., Lamb, A. L., O'Halloran, T. V., and Rosenzweig, A. C. (2000) Structural Basis for Copper Transfer by the Metallochaperone for the Menkes/Wilson Disease Proteins, *Nat. Struct. Biol. 7*, 766−771.
14. Anastassopoulou, A., Banci, L., Bertini, I., Cantini, F., Katsari, E., and Rosato, A. (2004) Solution Structure of the Apo and Copper(I)-Loaded Human Metallochaperone HAH1, *Biochemistry 43*, 13046−13053.
15. Ralle, M., Lutsenko, S., and Blackburn, N. (2003) X-ray absorption spectroscopy of the copper chaperone HAH1 reveals a linear 2-coordinate Cu(I) center capable of adduct formation with exogenous thiols and phosphines, *J. Biol. Chem. 278*, 23163−23170.
16. Gitschier, J., Moffat, B., Reilly, D., Wood, W. I., and Fairbrother, W. J. (1998) Solution structure of the fourth metal-binding domain from the Menkes copper-transporting ATPase, *Nat. Struct. Biol. 5*, 47−54.
17. Arnesano, F., Banci, L., Bertini, I., Huffman, D. L., and O'Halloran, T. V. (2001) Solution Structure of the Cu(I) and Apo Forms of the Yeast Metallochaperone, Atx1, *Biochemistry 40*, 1528−1539.
18. Larin, D., Mekios, C., Das, K., Ross, B., Yang, A., and Gilliam, T. C. (1999) Characterization of the Interaction between the Wilson and Menkes Disease Proteins and the Cytoplasmic Copper Chaperone, HAH1, *J. Biol. Chem. 274*, 28497−28504.
19. Arnesano, F., Banci, L., Bertini, I., and Bonvin, A. M. J. J. (2004) A docking approach to the study of copper trafficking proteins: Interaction between metallochaperones and soluble domains of copper ATPases, *Structure 12*, 669−676.
20. Banci, L., Bertini, I., Cantini, F., Felli, I. C., Gonnelli, L., Hadjiliadis, N., Pierattelli, R., Rosato, A., and Voulgaris, P. (2006) The Atx1-Ccc2 complex is a metal-mediated protein-protein interaction, *Nat. Chem. Biol. 2*, 367−368.
21. Cobine, P. A., and Winge, D. R. (2006) Visualizing tricoordinate copper transfer, *Nat. Chem. Biol. 2*, 352−353.
22. Comba, P., and Remenyi, R. (2002) A New Molecular Mechanics Force Field for the Oxidized form of Blue Copper Proteins, *J. Comput. Chem. 23*, 697−705.
23. Dalosto, S. D. (2007) Computer simulation of the interaction of Cu(I) with Cys residues at the binding site of the yeast metallochaperone Cu(I)-Atx1, *J. Phys. Chem. B 111*, 2932−2940.
24. Gresh, N., Policar, C., and Giessner-Prettre, C. (2002) Modeling Cu(I) Complexes: SIBFA Molecular Mechanics versus ab Initio Energetics and Geometrical Arrangements, *J. Phys. Chem. A 106*, 5660−5670.
25. Ungar, L. W., Scherer, N. F., and Voth, G. A. (1997) Classical molecular dynamics simulation of the photoinduced electron transfer dynamics of plastocyanin, *Biophys. J. 72*, 5−17.
26. Frisch, M. J., Trucks, G. W., Schlegel, H. B., Scuseria, G. E., Robb, M. A., Cheeseman, J. R., Zakrzewski, V. G., Montgomery, J. A., Jr., Stratmann, R. E., Burant, J. C., Dapprich, S., Millam, J. M., Daniel, A. D., Kudin, K. N., Strain, M. C., Farkas, Ö., Tomasi, J., Barone, V., Cossi, M., Cammi, R., Mennucci, B., Pomelli, C., Adamo, C., Clifford, S., Ochterski, J., Petersson, G. A., Ayala, P. Y., Cui, Q., Morokuma, K., Salvador, P., Dannenberg, J. J., Malick, D. K., Rabuck, A. D., Raghavachari, K., Foresman, J. B., Cioslowski, J., Ortiz, J. V., Baboul, A. G., Stefanov, B. B., Liu, G., Liashenko, A., Piskorz, P., Komáromi, I., Gomperts, R., Martin, R. L., Fox, D. J., Keith, T., Al-Laham, M. A., Peng, C. Y., Nanayakkara, A., Challacombe, M., Gill, P. M. W., Johnson, B., Chen, W., Wong, M. W., Andres, J. L., Gonzalez, C., Head-Gordon, M., Replogle, E. S., and Pople, J. A. (2003) *Gaussian 03*, version C.01, Gaussian, Inc., Pittsburgh, PA.
27. Becke, A. D. (1988) Density-functional exchange-energy approximation with correct asymptotic behavior, *Phys. Rev. A 38*, 3098−3100.
28. Hertwig, R. H., and Koch, W. (1997) On the parameterization of the local correlation functional. What is Becke-3-LYP? *Chem. Phys. Lett. 268*, 345−351.
29. Lee, C., Yang, W., and Parr, R. G. (1988) Development of the Colle-Salvetti correlation-energy formula into a functional of the electron density, *Phys. Rev. B 37*, 785−789.

30. Stephens, P. J., Devlin, F. J., Chabalowski, C. F., and Frisch, M. J. (1994) Ab Initio Calculation of Vibrational Absorption and Circular Dichroism Spectra Using Density Functional Force Fields *J. Phys. Chem. 98*, 11623−11627.
31. Gordon, M. S., Defrees, D. J., and Pople, J. A. (1982) Self-consistent molecular orbital methods. XXIII. A polarization-type basis set for second-row elements, *J. Chem. Phys. 77*, 3654−3665.
32. Hariharan, P. C., and Pople, J. A. (1973) The influence of polarization functions on molecular orbital hydrogenation energies, *Theor. Chem. Acc. 28*, 213−222.
33. Hehre, W. J., Ditchfield, R., and Pople, J. A. (1972) Self-Consistent Molecular Orbital Methods. XII. Further Extensions of Gaussian-Type Basis Sets for Use in Molecular Orbital Studies of Organic Molecules, *J. Chem. Phys. 56*, 2257−2261.
34. Olsson, M. H. M., and Ryde, U. (2001) Geometry, Reduction Potential, and Reorganization Energy of the Binuclear Cu_A Site, Studied by Density Functional Theory, *J. Am. Chem. Soc. 123*, 7866−7876.
35. Molecular Simulations, Inc. (2000) *WebLab ViewerPro*, version 3.7.
36. Besler, B. H., Merz, K. M. J., and Kollman, P. A. (1990) Atomic charges derived from semiempirical methods, *J. Comput. Chem. 11*, 431−439.
37. Singh, U. C., and Kollman, P. A. (1984) An approach to computing electrostatic charges for molecules, *J. Comput. Chem. 5*, 129−145.
38. Shannon, R. D. (1976) Revised effective ionic radii and systematic studies of interatomic distances in halides and chalcogenides, *Acta Crystallogr. A32*, 751−767.
39. Case, D. A., Darden, T. A., Cheatham, T. E. I., Simmerling, C. L., Wang, J., Duke, R. E., Luo, R., Merz, K. M. J., Pearlman, D. A., Crowley, M., Walker, R. C., Zhang, W., Wang, B., Hayik, S., Roitberg, A. E., Seabra, G., Wong, K. F., Paesani, F., Wu, X., Brozell, S., Tsui, V., Gohlke, H., Yang, L., Tan, C., Mongan, J., Hornak, V., Cui, G., Beroza, P., Mathews, D. H., Schafmeister, C., Ross, W. S., and Kollman, P. A. (2006) *AMBER*, version 9, University of California, San Francisco.
40. Cornell, W. D., Cieplak, P., Bayly, C. I., Gould, I. R., Merz, K. M., Ferguson, D. M., Spellmeyer, D. C., Fox, T., Caldwell, J. W., and Kollman, P. A. (1995) A second generation force field, *J. Am. Chem. Soc. 117*, 5179−5197.
41. Berendsen, H. J. C., Postma, J. P. M., van Gunsteren, W. F., DiNola, A., and Haak, J. R. (1984) Molecular dynamics with coupling to an external bath, *J. Chem. Phys. 81*, 3684−3690.
42. Pufahl, R. A., Singer, C. P., Peariso, K. L., Lin, S.-J., Schmidt, P. J., Fahrni, C. J., Culotta, V. C., Penner-Hahn, J. E., and O'Halloran, T. V. (1997) Metal ion chaperone function of the soluble Cu(I) receptor Atx1, *Science 278*, 853−856.

BI7007195